CHAPTER

20 INTRAVASCULAR ULTRASOUND IMAGING OF HUMAN CORONARY ATHEROSCLEROTIC PLAQUE: NOVEL MORPHO-ELASTIC BIOMARKERS OF INSTABILITY

Armida Gómez[1], Antoine Tacheau[1], Simon Le Floc'h[2], Roderic I. Pettigrew[3,4], Guy Cloutier[5], Gérard Finet[6], Jacques Ohayon[1,7]

[1]*Laboratory TIMC-IMAG, CNRS UMR 5525, Grenoble-Alpes University, Grenoble, France;* [2]*Laboratory LMGC, CNRS UMR, University of Montpellier II, Montpellier, France;* [3]*Texas A&M University and Houston Methodist Hospital, Houston, TX, United States;* [4]*CEO, Engineering Health (EnHealth) and Executive Dean, Engineering Medicine (EnMed), Houston, TX, United States;* [5]*Laboratory of Biorheology and Medical Ultrasonics, University of Montreal Hospital Research Center (CRCHUM), Montréal, QC, Canada;* [6]*Hospices Civils de Lyon, Department of Interventional Cardiology, Cardiovascular Hospital and Claude Bernard University and INSERM Unit 1060 CARMEN, Lyon, France;* [7]*Communauté Université Grenoble-Alpes, Savoie Mont-Blanc University, Polytech Annecy-Chambéry, Le Bourget du Lac, France*

ABBREVIATIONS

AI	Anisotropy index
DWS	Dynamic watershed segmentation
iMOD	Imaging modulography
iPALP	Imaging palpography
IVUS	Intravascular ultrasound
LSME	Lagrangian speckle model estimator
MST	Modified Sumi's transform
PCS	Thin-cap fibroatheroma peak cap stress
PFEM	Parametric finite element model
PVA	Polyvinyl alcohol
RF	Radio frequency
RMS	Root mean square
VP	Vulnerable plaque

Biomechanics of Coronary Atherosclerotic Plaque. https://doi.org/10.1016/B978-0-323-85933-2.00020-2

1. INTRODUCTION

According to clinical, pathological, and biomechanical studies, the criteria that define a vulnerable coronary atherosclerotic plaque (VP) are strongly linked to its morphology and composition (Fleg et al., 2012; Naghavi et al., 2003; Virmani et al., 2000). Macrophage accumulation, large necrotic core with a thin fibrous cap (<65 μm), and positive remodeling are common morphological characteristics of inflammatory atherosclerotic lesions susceptible to rupture. Several techniques enable the imaging of atherosclerotic plaques, including intravascular ultrasound (IVUS) (Cheng et al., 2014; Rioufol et al., 2002), optical coherence tomography (Gessert et al., 2018; Sinclair et al., 2015), computed tomography (Fayad et al., 2002), and magnetic resonance imaging (Cavalcante and Larose, 2016; Larose et al., 2005), as well as hybrid techniques resulting from the combination of two or more imaging modalities (Bourantas et al., 2017; Abran et al., 2014). Despite all these advances toward diagnosing plaques, classifying them as vulnerable and ultimately identifying patients at high risk of adverse coronary events remains an ongoing challenge.

Fibrous cap thickness (Cap_{thick}) is often regarded as a good predictor of plaque stability (Virmani et al., 2000; Virmani, 2011). However, even a significant criterion for rupture as cap thickness is not enough to give a definite assessment by itself. A study conducted by Virmani et al. (2000) involving 200 cases of sudden death evidenced that, while most culprit lesions (60%) were ruptured thin-cap fibroatheromas, 70% of these patients also presented unruptured lesions with similar morphologies. This suggests that cap thickness by itself cannot predict the likelihood of rupture, and that other morphological and biomechanical characteristics must come into play.

To predict plaque instability, novel in vivo clinical imaging tools must be developed to simultaneously assess plaque morphology (Fleg et al., 2012; Farb et al., 1996) and mechanical properties of all atherosclerotic lesion constituents (Ohayon et al., 2012). This could improve the approximation of the thin-cap fibroatheroma peak cap stress (PCS), a key biomechanical rupture-risk parameter, obtained through the use of the finite element method in structural mechanics (Ohayon et al., 2001, 2008; Finet et al., 2004; Loree et al., 1992; Lee et al., 1993). Results presented in Chapter 16 of this volume show that mechanical stress in coronary plaques is maximal at high elasticity gradient zones and more specifically at the interface between cap and necrotic core in the plaque shoulder regions, making this location a potential source of fissure or vulnerability. Moreover, the PCS may be significantly altered when local microcalcifications are present in the thin fibrous cap (Cardoso and Weinbaum, 2018, chapter 17 of this volume; Maldonado et al., 2013). In vitro experiments performed on human pathological coronary arteries have shown that intimal tissue rupture occurs at circumferential stress levels near 394 ± 223 kPa (Holzapfel et al., 2005).

When encountering a coronary lesion, the interventional cardiologist must analyze if the risk of rupture it poses is significant enough to treat the patient using a surgical or percutaneous revascularization approach. Although helpful, the patient's medical history and paraclinical tests are not enough to give an adequate prognosis due to the unpredictable clinical course of atherosclerotic lesions. Clinical imaging methods have a great potential for improving the crucial in vivo detection and evaluation of VPs. Therefore, the development and validation of novel elasticity imaging tools and their implementation on routine clinical examinations could be a valuable contribution toward proper plaque assessment (Fleg et al., 2012).

Following this premise, several approaches to detect vulnerable plaques based on the determination of their elastic properties have been proposed (Doyley, 2012). In 2004, the virtual histology technique,

based on the parametric spectral analysis of the radio-frequency ultrasound backscattered echoes, was developed by Volcano Therapeutics Inc. However, in the study by Thim et al. (2010) performed on adult atherosclerosis-prone minipigs, no correlation was found between necrotic core size determined by virtual and real histology, questioning the ability of virtual histology to detect rupture-prone plaques. Moreover, this technique does not allow an accurate quantification of the mechanical properties of the plaque constituents, which is essential for the computation of intraplaque stress distribution. The same year, our joint laboratories developed a robust IVUS strain-elastography approach (named EVE for EndoVascular Elastography), based on an optical flow method to estimate the radial strain wall induced by the natural cardiac pulsatile blood pressure (Maurice et al., 2004a,b). However, this method did not overcome a main limitation related to the complex geometries of atherosclerotic plaques, which alter the intraplaque strain fields and inhibit a direct translation into plaque mechanical properties.

Several computational algorithms have been developed to attempt the reconstruction of elasticity maps within the arterial wall based on the estimation of the strain field obtained with various IVUS-based techniques (Maurice et al., 2004a,b; De Korte et al., 2002). Either direct (Kim et al., 2004; Kanai et al., 2003) or iterative (Baldewsing et al., 2008; Luo et al., 2006) numerical procedures were used. Iterative methods depend mainly on two crucial elements: the performance of the optimization algorithm that minimizes the error between the calculated and the measured strain or displacement fields and the precision of the contours of the plaque constituents. This has led to the development of several robust optimization algorithms to compute the elastic moduli of the plaque components assuming a known plaque morphology (Khalil et al., 2006; Soualmi et al., 1997). Another interesting solution was developed (Baldewsing et al., 2006) and extended (Baldewsing et al., 2007) by Van der Steen's group. It consisted of detecting lipid core contours, analyzing each inclusion separately, and superposing these results to obtain the final mechanical solution. Regardless of the robustness of the approach, it inherently neglected the mechanical interactions between inclusions, hindering the accuracy of the results in cases with neighboring inclusions, thus affecting the vulnerability prediction.

Since 2009, significant improvements have been performed and two powerful IVUS biomarkers of coronary plaque instability (namely iPALP and iMOD for imaging palpography and modulography (or morpho-elasticity), respectively) were developed in our joint laboratories (Gómez et al., 2019; Tacheau et al., 2016; Bouvier et al., 2013; Deleaval et al., 2013; Le Floc'h et al., 2012, 2010, 2009).

A thorough review and classification of IVUS imaging models is beyond the scope of this work. In this chapter, we present our two most recent IVUS imaging techniques developed for the in vivo detection and mechanical characterization of vulnerable coronary atherosclerotic plaques.

2. INTRAVASCULAR ULTRASOUND IMAGE ANALYSIS

2.1 INTRAVASCULAR ULTRASOUND STRAIN-ELASTOGRAPHY

In our two modeling approaches (i.e., iPALP and iMOD), the strain of the atherosclerotic plaque between two consecutive images ($\mathbf{Im^i}$ and $\mathbf{Im^{i+1}}$) was obtained by considering the geometry of the lesion at $\mathbf{Im^i}$ as the reference configuration. First, the segmentation of the vessel boundaries (i.e., the lumen and the external adventitia) was performed on the IVUS images using a fast-marching algorithm that combined region and contour information (Roy Cardinal et al., 2006); the resulting contours were then corroborated by a cardiologist before proceeding. These contours delimitating the arterial

wall determined the region of interest (ROI). Then, a rigid motion compensation was applied to the IVUS sequence to dismiss the rotation observed between consecutive images. To do this, the polar representations of each pair of successive frames $\mathbf{Im^i}$ and $\mathbf{Im^{i+1}}$ was compared using a 2D correlation of the ROI, and the shift with the maximal correlation was selected as the correcting angular compensation to avoid the rotation artifact. This step was repeated until the complete sequence was compensated for rotation. Finally, the radial strain was calculated using the Lagrangian speckle model estimator (LSME) (Maurice et al., 2004a,b). This algorithm consists of dividing the IVUS image within the ROI into a series of overlapping subwindows (or measurement windows, MWs) and then calculates the displacement of each MW between $\mathbf{Im^i}$ and $\mathbf{Im^{i+1}}$ using a 2D cross-correlation analysis, thus computing a displacement field. The LSME algorithm was formulated as a nonlinear minimization problem based on the optical flow equations solved for each MW and allows direct assessment of the spatial IVUS radial strain distribution $\left(\varepsilon_{RR}^{LSME}\right)$ (Maurice et al., 2004a,b). The detailed description of the LSME strain elastography algorithm including its governing equations has been published by our group (see Appendix A in Majdouline et al. (2014)).

2.2 TANGENT STIFFNESS MATRIX OBTAINED FROM TWO CONSECUTIVE INTRAVASCULAR ULTRASOUND IMAGES

As explained previously, the proposed constitutive model takes the plaque configuration at the preceding frame $\mathbf{Im^i}$ as the reference, and not the zero-stress configuration $\mathbf{R}$. Consequently, we used a linear tangent elasticity procedure (Holzapfel, 2000), which remains valid as long as the absolute local incremental strain amplitudes between the two consecutive IVUS images $\mathbf{Im^i}$ and $\mathbf{Im^{i+1}}$ are $<2\%$.

The relationship between the second Piola-Kirchhoff stress $\mathbf{S}$ and the right Cauchy-Green tensor $\mathbf{C}$ (or the Lagrangian strain tensor $\mathbf{E} = (\mathbf{C} - \mathbf{I})/2$) is nonlinear:

$$\mathbf{S} = 2\frac{\partial \psi}{\partial C} = \frac{\partial \psi}{\partial E} \tag{20.1}$$

where ψ is the strain energy function per unit of undeformed volume (i.e., at configuration $\mathbf{R}$ associated to coordinates X). This relationship could be linearized with respect to an incremental displacement $\mathbf{u}$ defining the transformation going from $\mathbf{Im^i}$ to $\mathbf{Im^{i+1}}$ (Bonet and Wood, 1997):

$$\mathrm{D}\mathbf{S}[\mathbf{u}] = C^{\mathrm{Im^i}\rightarrow\mathrm{Im^{i+1}}} : \mathrm{D}\mathbf{E}[\mathbf{u}] \tag{20.2a}$$

with

$$\mathrm{D}\mathbf{E}[\mathbf{u}] = \mathbf{F}_{\mathrm{R}\rightarrow\mathrm{Im^i}}^{\mathrm{T}}\boldsymbol{\varepsilon}(\mathbf{u})\mathbf{F}_{\mathrm{R}\rightarrow\mathrm{Im^i}} \quad \text{and} \quad \boldsymbol{\varepsilon}(\mathbf{u}) = \left[\nabla\mathbf{u} + (\nabla\mathbf{u})^{\mathrm{T}}\right]/2 \tag{20.2b,c}$$

where ∇ indicates the gradient with respect to the coordinates at the current configuration $\mathbf{Im^i}$ (i.e., $\mathbf{x}$), $\boldsymbol{\varepsilon}(\mathbf{u})$ is the small strain tensor, $\mathrm{D}\mathbf{S}[\mathbf{u}]$ is the resulting incremental second Piola-Kirchhoff stress, and $C^{\mathrm{Im^i}\rightarrow\mathrm{Im^{i+1}}}$ is the symmetric fourth-order material elasticity tensor. In particular, if we assume that $\mathbf{Im^i}$ is the initial material configuration $\mathbf{R}$ (i.e., when $\mathbf{x} = \mathbf{X}$ and therefore $\mathbf{F}_{\mathrm{R}\rightarrow\mathrm{Im^i}} = \mathbf{I}$), the linearization of Eqs. (20.2a–c) yields to the classical linear elastic constitutive law:

$$S(\mathbf{u}) = C^{\mathrm{Im^i}\rightarrow\mathrm{Im^{i+1}}} : \boldsymbol{\varepsilon}(\mathbf{u}) \tag{20.3}$$

Therefore, our computations were performed assuming linear elastic tissue response (i.e., $C^{Im^i \rightarrow Im^{i+1}}$ remains constant) when the artery was pressurized with a small incremental blood pressure $\Delta P^{Im^i \rightarrow Im^{i+1}}$ and under plane strain condition. Interestingly, this incremental procedure applied to a series of two consecutive IVUS images ($\mathbf{Im^i}$, $\mathbf{Im^{i+1}}$ with i = 1 to n) during the entire cardiac cycle sequence allowed to highlight the nonlinear mechanical response of the plaque media (Le Floc'h et al., 2012).

3. THE PALPATION TECHNIQUE *iPALP* FOR PLAQUE ANISOTROPY CHARACTERIZATION

Two decades ago, Van der Steen's group was the first to propose an elasticity palpography technique for estimating the apparent stress-strain modulus of the arterial wall layer (Céspedes et al., 2000). Their model was based on the mechanical behavior of a circular and concentric vascular wall and used IVUS strain measurements as inputs. Later, our group improved this approach by considering realistic anatomical cross-sectional shapes of atherosclerotic lesions (Deleaval et al., 2013). Despite the promising results of these VP detection tools, they have suffered from the limitation of considering tissues as isotropic materials. To overcome this, a subsequent study was designed by accounting for the orthotropic mechanical properties of the arterial wall and lesion constituents (Gómez et al., 2019). An elastic anisotropy index (AI) was defined based on the continuum mechanics theory. This novel anisotropic elasticity-palpography technique—successfully applied to characterize atherosclerotic coronary plaques and healthy vessels of patients imaged in vivo with IVUS—is presented below.

3.1 FORWARD PROBLEM: STRAIN FIELD DISTRIBUTION OBTAINED FROM RECONSTRUCTED IVUS IMAGES

In this work, simulated IVUS images were used to test the accuracy and validate the performance of the proposed inverse anisotropic elasticity-palpography technique. Fig. 20.1 illustrates the different steps performed to reconstruct the IVUS radial strain-elastograms.

Finite element model. The 2D contours extracted from the IVUS image (i.e., $R = R_i(\theta)$ and $R = R_e(\theta)$ where $R_i(\theta)$ and $R_e(\theta)$ are the inner and outer radii of the artery cross section) were introduced into Comsol finite element (FE) software (Structural Mechanics Module, version 4.3b, Comsol, France), using the barycenter of the lumen area as the origin of the cylindrical coordinate system (R, θ, Z). The resulting cross-sectional profile of the plaque was extruded in the longitudinal direction of the artery to create a 3D thin-sliced plaque (thickness = 0.1 mm) geometry. Then, the deformed shape was computed with a simulation using this 3D geometry meshed with six-node prism elements (∼5000). A blood pressure differential amplitude ΔP was applied at the lumen boundary. Since instantaneous pressures were not recorded along with the IVUS acquisitions, a blood pressure differential amplitude ΔP between 0.3 and 1 kPa (i.e., 2.2−7.5 mmHg) was assumed, corresponding to a realistic pressure gradient between two successive IVUS frames (Le Floc'h et al., 2012, 2010, 2009).

The external artery wall $(R = R_e(\theta))$ had free boundary condition and the two cross sections of the vessel segment (R-θ planes, Z = 0 and 0.1 mm) were constrained with sliding conditions, so that the deformation would take place only in the R-θ planes. In addition, the external nodes located on the four cardinal directions (i.e., at $R = R_e(k\pi/2)$ with k = 1 to 4) were subjected to circumferential displacement limitations to avoid rigid rotations, resulting in more realistic inflation kinematics by allowing free radial expansion of the wall during loading.

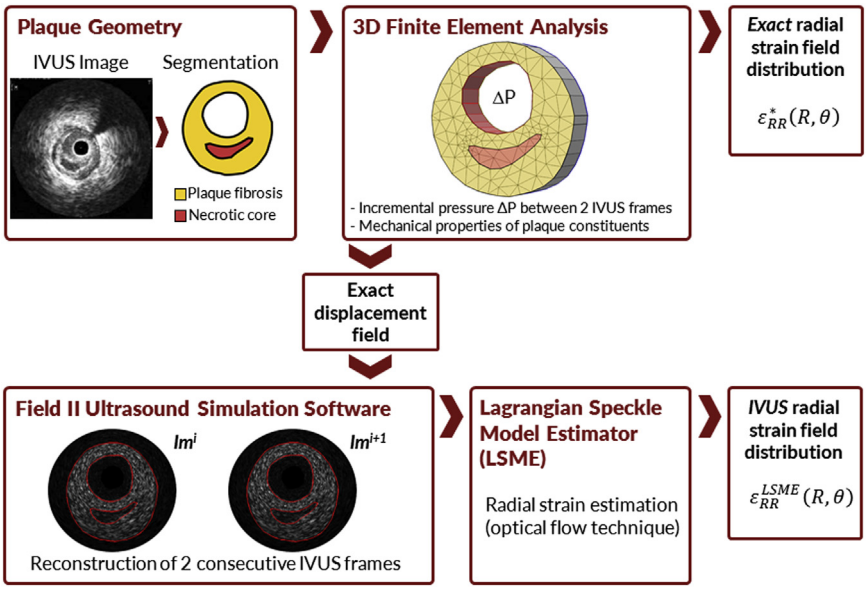

FIGURE 20.1

Illustration of the different calculation steps performed to reconstruct the acoustic radio frequency intravascular ultrasound (RF-IVUS) images and to extract the LSME spatial distribution of radial deformation ($\boldsymbol{\varepsilon}_{RR}^{LSME}$) from these simulated RF-IVUS data (see Section 3.1 for more details).

The pathological vessels are composed of fibrous and soft necrotic tissues. The fibrotic plaque was considered as orthotropic (Berthelot, 1999) and quasi-incompressible with initial mechanical properties coming from measurements performed on thick intima layers of nonatherosclerotic human coronaries (Holzapfel et al., 2005; Chagnon et al., 2017). Soft necrotic core inclusions were modeled as isotropic and quasi-incompressible (Lee et al., 1991). Mechanical properties for these media are summarized in Table 20.1.

Simulation of IVUS images. To reconstruct the IVUS images, the open source software Field II (Jensen and Svendsen, 1992) was used (Nayak et al., 2017; Poree et al., 2017; Fromageau et al., 2003) (Fig. 20.1). Since each biological tissue has a distinct scattering amplitude, acoustic models were built by randomly distributing scatterers over each nondeformed medium and adjusting the relative acoustic scatterer amplitudes of blood, necrotic core, and fibrotic plaque to 10%, 15%, and 35%, respectively (Maurice et al., 2004a,b Le Floc'h et al., 2010; Cardoso et al., 2012). To simulate two consecutive IVUS images, first, we created an IVUS image of the initial nondeformed state (i.e., Im^{i}). Then, using the displacement from the FE simulation, the scatterers were repositioned to reconstruct the image after the load is applied (i.e., Im^{i+1}). A single rotating piezo-electric element (600 μm diameter, 40 MHz central emission frequency) was modeled. An incremental circumferential rotation step of 0.7 degrees was set to get 512 lines of radio frequency (RF) signal for IVUS image reconstruction. A sampling frequency of 400 MHz was mimicked to represent the RF signal (SVMI HD-IVUS system ACIST Medical Systems, Eden Prairie, MN, USA). In these simulations, we assumed the centroid of

Table 20.1 Orthotropic and isotropic mechanical properties and anisotropic index values AI assigned to the quasi-incompressible fibrous plaque and soft necrotic inclusion media for our finite element simulations.

	Young's moduli (kPa)			Poisson's ratios			Shear moduli (kPa)	Anisotropic index (kPa)
Reference (*medium*)	E_R	E_θ	E_Z	$\nu_{R\theta}$	ν_{RZ}	$\nu_{\theta Z}$	$G_{R\theta} = G_{RZ} = G_{\theta Z}$	**AI**
Fibrous plaque (*intima*) (Holzapfel et al., 2005)	360	230	330	0.7370	0.5289	0.2627	30	384.3
Necrotic core[a] (Loree et al., 1994)	5			0.49				6.7

[a] *Isotropic ($E_R = E_\theta = E_Z$ and $\nu_{R\Theta} = \nu_{RZ} = \nu_{\Theta Z}$).*
Adapted from Gómez, A., Tacheau, A., Finet, G., Lagache, M., Martiel, J.L., Floc'h, S.L., et al., 2019. Intraluminal ultrasonic palpation imaging technique revisited for anisotropic characterization of healthy and atherosclerotic coronary arteries: a feasibility study. Ultrasound Med Biol 45 (1), 35–49.

the lumen coincident with the probe location. These sequences of simulated HD-IVUS images were then processed using the LSME algorithm presented in Section 2.1 of this chapter.

3.2 INVERSE PROBLEM: THE ANISOTROPIC ELASTICITY-PALPOGRAPHY MODEL

The elastic AI was defined as the ratio of the averaged difference between the radial and circumferential stresses (σ_{RR} and $\sigma_{\theta\theta}$, respectively) over the averaged radial strain (ε_{RR}) along the radial axis:

$$AI(\theta) = \frac{\left| \int_{R_i(\theta)}^{R_o(\theta)} \{\sigma_{RR}(R,\theta) - \sigma_{\theta\theta}(R,\theta)\} dR \right|}{\varepsilon(\theta)} \tag{20.4}$$

with

$$\varepsilon(\theta) = \left| \int_{R_i(\theta)}^{R_o(\theta)} \varepsilon_{RR}(R,\theta) dR \right| \tag{20.5}$$

where $R_i(\theta)$ and $R_o(\theta)$ are the inner and outer radii of the considered palpography domain (Ω_{palpo}), respectively. A detailed description of the derivation of this index has been published by our group (see Appendix II in Gómez et al. (2019)).

Notice that, when considering a homogeneous pathological lesion made of the same quasi-incompressible orthotropic medium (i.e., when $E_R(R,\theta) = E_R^0$, $E_\theta(R,\theta) = E_\theta^0$ and $E_Z(R,\theta) = E_Z^0$, whatever the values of R and θ), the amplitude of AI(θ) remains constant and equal to

$$AI = E_R^0 \left[1 - \frac{1}{4} \left(1 - \frac{E_R^0}{E_\theta^0} + \frac{E_R^0}{E_Z^0} \right) \left(1 + \frac{E_Z^0}{E_R^0} - \frac{E_Z^0}{E_\theta^0} \right) \right]^{-1} \tag{20.6}$$

This relationship remains true regardless of the geometry of the plaque and the palpography domain considered Ω_{palpo}.

For a homogeneous incompressible transversely isotropic lesion (i.e., when $E_R(R,\theta) = E_R^0$ and $E_Z(R,\theta) = E_\theta(R,\theta) = E_\theta^0$, whatever the values of R and θ), the AI amplitude is reduced to the following constant:

$$AI = \frac{4E_R^{0^2}}{4E_R^0 - E_\theta^0} \tag{20.7}$$

and finally to $AI = 4E_{isotropic}/3$ for a homogeneous incompressible isotropic plaque (i.e., when $E_R(R,\theta) = E_\theta(R,\theta) = E_Z(R,\theta) = E_{isotropic}$). Table 20.1 gives the amplitudes of the anisotropy index AI for the considered mechanical properties of the fibrotic plaque and soft necrotic core.

3.3 QUANTIFYING THE ACCURACY OF THE ANISOTROPIC ELASTICITY-PALPOGRAPHY MODEL

To investigate the accuracy of the AI-palpogram, we compared it to the exact palpogram (AI^{exact}), which is obtained by computing the circumferential distribution of the averaged anisotropic material constant $C(R,\theta)$ along the radial axis:

$$AI^{exact}(\theta) = \frac{1}{R_o(\theta) - R_i(\theta)} \int_{R_i(\theta)}^{R_o(\theta)} C(R,\theta) dR \tag{20.8}$$

where

$$\sigma_{RR}(R,\theta) - \sigma_{\theta\theta}(R,\theta) = C(R,\theta)\varepsilon_{RR}(R,\theta) \tag{20.9}$$

To quantify the cumulative error induced by both the proposed palpography technique and the estimated IVUS-radial strain-elastogram, the following mean relative anisotropy index error MR_{error}^{AI} was defined:

$$MR_{error}^{AI}(\%) = \frac{100}{2\pi} \int_{\theta=0}^{2\pi} \left| \frac{AI(\theta) - AI^{exact}(\theta)}{AI^{exact}(\theta)} \right| d\theta \tag{20.10}$$

3.4 RESULTS AND DISCUSSION: THE PALPOGRAPHY IMAGING TOOL

Two studies were conducted to test and validate the performance of the AI-palpography-imaging tool. In the first one (i.e., the feasibility study), the imaging technique was applied to several sequences of

reconstructed HD-IVUS images of human coronary plaques, while in the second study, real IVUS acquisitions and ex-vivo experiments were conducted on rabbit aortas.

The feasibility study. The anisotropic palpography technique was applied to a series of seven geometries obtained from patients who underwent coronary IVUS at the Louis Pradel Cardiology Hospital of Lyon (France) after a first acute coronary syndrome with troponin I elevation. Patients' consent was obtained, and this study was approved by the ethical institutional review board of the hospital.

One homogeneous eccentric atherosclerotic fibrous plaque geometry was used to validate the proposed anisotropic elasticity-palpography technique (plaque #11, Fig. 20.2A–C). As expected, the AI-palpogram remains almost constant whatever the angular position and a good accuracy between the estimated (i.e., 360 ± 15 kPa) and the exact (i.e., 384.3 kPa) mean (±SD) AI amplitudes was found. Additional simulations were performed on human VPs with one and two necrotic cores (plaques #14 and #16, Fig. 20.2D–I). The obtained AI-palpograms successfully identified the locations of the soft inclusions and characterized quite accurately the change in the orthotropic material properties from the fibrous to the soft tissues (Fig. 20.2D–I). For these vulnerable plaques, the mean (±SD) amplitudes of the estimated AI-palpograms (i.e., plaque #14: 392 ± 30 kPa and plaque #16: 385 ± 25 kPa) were close to the theoretical AI value of the fibrotic plaque (i.e., 384.3 kPa) at the inclusion-free angular regions. Moreover, as expected, the estimated AI value was significantly lower at the locations where the soft inclusions were present (see Fig. 20.2F and I). In total, the mean relative error MR_{error}^{AI} for all atherosclerotic cases (n = 7) was of 36.94 ± 60.97%, and the necrotic cores were accurately detected for these seven VPs considered.

This new IVUS palpation imaging technique allows a proper quantification of the anisotropic arterial wall apparent stiffness using IVUS radial strain field and blood pressure data. The AI-palpogram is highly responsive to mechanical heterogeneities, effectively capturing the drop in mechanical properties when encountering soft inclusions within the atherosclerotic lesion (Fig. 20.2D–I). An interesting aspect of the AI index is that it incorporates the Young's moduli of the plaque constituents and, although it cannot identify them individually, it can give some insight into the relationships between them. The AI is proportional to the radial Young's modulus and depends on the two stiffness ratios $k_1 = E_\theta/E_R$ and $k_2 = E_Z/E_R$. More specifically, Eq. (20.6) shows that an increase of AI may be due to either an increase of E_R and E_Z or a decrease of E_θ.

Animal study: Ex vivo experiment. Experiments were performed on healthy aortas to acquire RF-IVUS sequences, histologic data, and elasticity measurements from the same arterial section. Animal population consisted of two Watanabe rabbits. Rabbit aortas have similar dimensions to those of human coronaries (Abela et al., 2016). The following protocol was conducted. After general anesthesia, rabbits were euthanized, and the thoracic and abdominal aortas were immediately harvested in a 4°C Krebs-Henseleit (KH) solution. The length of the samples was measured before excision in order to later reproduce the longitudinal in situ stretch of the artery on the experimental bench. The surrounding tissue was removed after dissection and the arteries were submerged on the KH solution bath during all manipulations to avoid tissue deterioration. Later, the arterial sections were mounted on an experimental bench to acquire IVUS images with pressure recordings. The IVUS platform used to record the RF signal was the GALAXY2 (Boston Scientific, Watertown, MA) equipped with a 30 MHz Atlantis SR Pro 3.6 F catheter. Dynamic pressure profiles of small amplitudes were applied for the image acquisitions; the results presented here were extracted from sequences with cyclic sinusoidal dynamic pressure at 30 beats per minute (peristaltic pump model

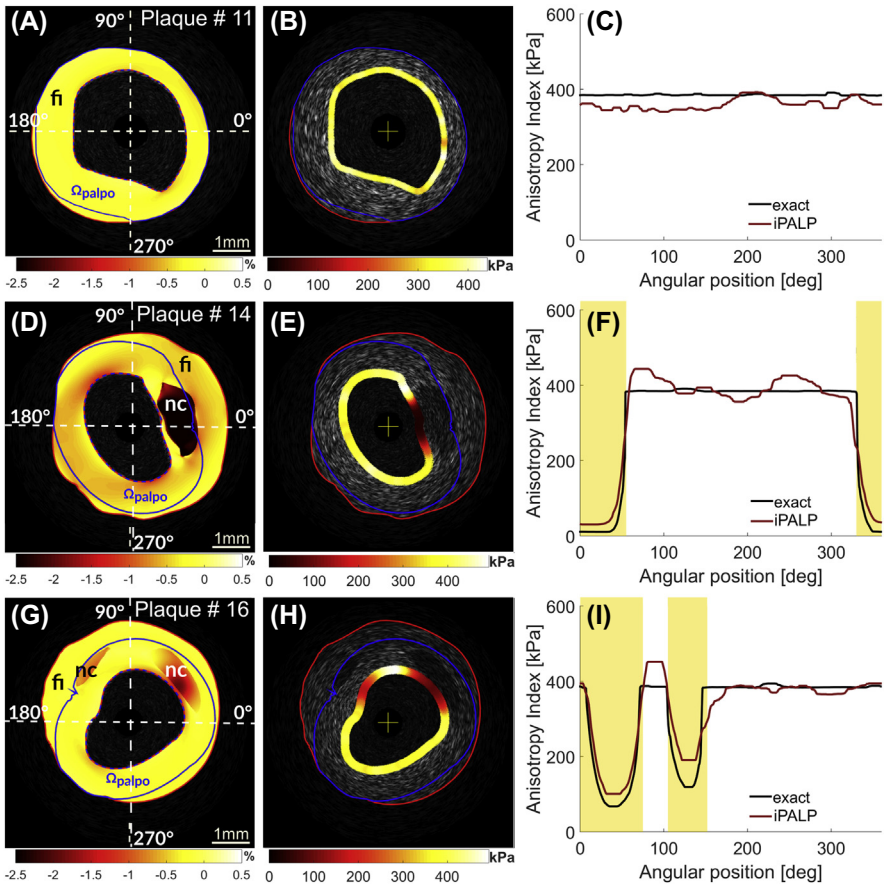

FIGURE 20.2

Performance of the anisotropic elasticity-palpography algorithm iPALP to detect and characterize the mechanical properties of human coronary atherosclerotic plaques using reconstructed-IVUS images. (A–C) Nonvulnerable fibrous plaque (plaque #11); (D–F) vulnerable plaque with one necrotic core (plaque #14); (G–I) vulnerable plaque with two necrotic cores (plaque #16). (A, D, G) Plaque geometries (red contours), palpography domains (blue contours), and estimated LSME radial strain-elastograms. (B, E, H) IVUS images with AI-palpograms. (C, F, I) Comparisons between exact and estimated (curve iPALP) AI(θ) palpograms. Areas shaded in yellow indicate the locations of the necrotic cores.

Adapted from Gómez, A., Tacheau, A., Finet, G., Lagache, M., Martiel, J.L., Floc'h, S.L., et al., 2019. Intraluminal ultrasonic palpation imaging technique revisited for anisotropic characterization of healthy and atherosclerotic coronary arteries: a feasibility study. Ultrasound Med Biol 45 (1), 35–49.

1405 PBP, Harvard Apparatus, USA). The maximal and minimal mean cyclic pressure amplitudes were of 2.10 and 2.60 kPa, and a mean incremental pressure amplitude ΔP close to 0.025 kPa was used to extract a series of 300 sets of two consecutive RF-IVUS images ($\mathbf{Im^i}$, $\mathbf{Im^{i+1}}$ with i = 1 to 300). This results in small displacements and allows the use of the small strain hypothesis (see

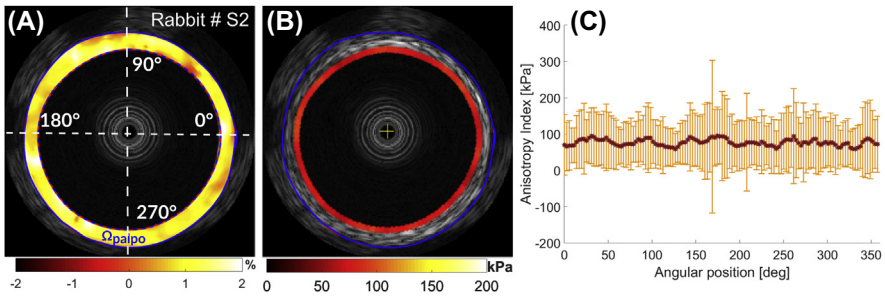

FIGURE 20.3

Performance of the anisotropic elasticity-palpography algorithm iPALP to characterize ex vivo a healthy aortic wall of a Watanabe rabbit (Rabbit #S2) using experimental RF-IVUS images acquired with a Boston Scientific GALAXY2 IVUS system. (A) Vessel geometry (*red* contours), palpography domain (*blue* contour), and estimated LSME radial strain-elastogram. (B) One IVUS image of the IVUS sequence with mean AI-palpogram. (C) Mean estimated AI-palpogram with its standard deviation. A series of n = 296 AI-palpograms were computed based on a recorded IVUS sequence of 300 images.

Section 2.2). Even though these do not represent in vivo and pathological conditions, they allow the evaluation of the AI-palpography algorithms' capabilities to extract the elasticity of the arterial tissues. After the IVUS acquisitions, sections of 10 and 16 microns (selected in the IVUS-imaged zone) were obtained with a microtome to be used in atomic force microscopy (AFM) and immunohistological stainings. Mechanical testing was performed on several sites over the arterial wall cross sections with a servo-controlled AFM (Nanowizard II, JPK instruments, Berlin, Germany). Serial 16 μm-thick vessel sections were mounted on Poly-L-lysine slides (Thermo-Scientific, France). The arterial walls, including the intima and media layers, were exposed for probing by AFM. Tissue samples were kept in KH buffer. All AFM measurements were made in liquid at room temperature, including cantilever calibration. For all specimens, mechanical testing was completed within 4 hours of harvesting the sample (a detailed description of the AFM protocol is given in Tracqui et al. (2011)). The AFM experimental protocol allows only the characterization of the initial Young's modulus in the longitudinal axis direction of the vessel (i.e., E_z). Therefore, we referred to the literature published on rabbit to (1) extract an estimate of the two other initial Young's moduli, namely in the circumferential (close to $E_\theta = 90$ kPa; see Fig. 20.3 in Hasegawa and Watanabe (1988)) and radial ($E_R = 42.8 \pm 3.7$ kPa; see Fig. 20.4 in Matsumoto et al. (2002)) directions, and (2) to confirm that our measured mean longitudinal Young's modulus value E_z is in agreement with published results by Hasegawa and Watanabe ($E_z = 80$ kPa; see Fig. 20.3 in Hasegawa and Watanabe (1988)). Biological characterization was achieved by means of two different histologic staining methods: hematoxylin eosin saffron (HES) trichromatic staining and Oil Red O.

Fig. 20.3 presents the resulting mean AI-palpogram computed for the healthy thoracic rabbit aortic cross section #S2. To check the reproducibility and the performance of the anisotropic elasticity-palpography technique we computed n = 296 AI-palpograms from a sequence of 300 IVUS images. The amplitude of the mean AI has been found to be quasi-uniform (76.7 ± 9.1 kPa). This mean AI value was compared to AI = 94.8 kPa, which is the value calculated (using Eq. 20.6) by considering the mean value of the longitudinal Young's moduli measured by AFM (i.e., $E_z = 53.4 \pm 60.1$ kPa) and

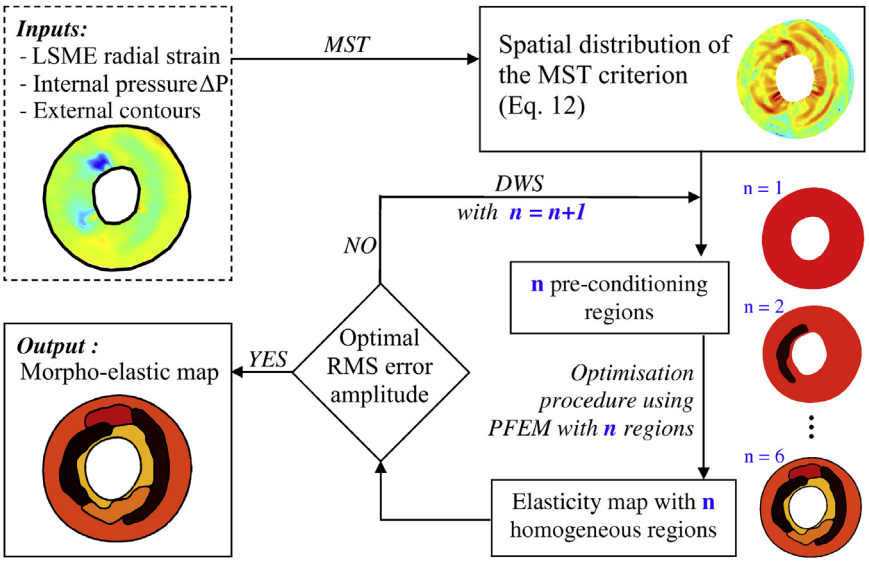

FIGURE 20.4

Illustration of the successive calculation steps performed in our plaque elasticity reconstruction algorithm iMOD based on a segmentation-driven optimization procedure using LSME strain measurements. *DWS*, dynamic watershed segmentation; *LSME*, Lagrangian speckle model estimator; *MST*, modified Sumi's transform; *PFEM*, parametric finite element model; *RMS*, root mean square (see Section 4.1 for more details).

Adapted from Le Floc'h, S., Cloutier, G., Finet, G., Tracqui, P., Pettigrew, R.I., Ohayon, J., 2010. On the potential of a new IVUS elasticity modulus imaging approach for detecting vulnerable atherosclerotic coronary plaques: in vitro vessel phantom study. Phys Med Biol 55, 5701–5721. © Institute of Physics and Engineering in Medicine. Reproduced by permission of IOP Publishing. All rights reserved.

the published amplitudes of the circumferential and radial Young's moduli $E_\theta = 90$ kPa and $E_R = 42.8$ kPa, respectively. It should also be noted that the amplitudes of the longitudinal Young's moduli measured by AFM ($E_z = 53.4 \pm 60.1$ kPa) are of the same order of magnitude as that measured by Hasegawa and Watanabe (1988) ($E_z = 80$ kPa).

All together, these previous results demonstrate the promising benefit of the anisotropic elasticity-palpography computer-assisted imaging tool iPALP to perform in vivo detection and quantitative characterization of healthy and pathological arteries.

4. THE MORPHO-ELASTIC BIOMARKER *iMOD*

Morpho-elastic reconstruction of atherosclerotic lesions (i.e., modulogram), based solely on radial strain field measurement, was a challenge addressed by several authors (Doyley, 2012; Baldewsing et al., 2005, 2008; Richards and Doyley, 2011). Our group demonstrated that by preconditioning the algorithm based on the best estimate of the boundaries of all plaque components, we could improve the elasticity reconstruction (Tacheau et al., 2016; Le Floc'h et al., 2012, 2010, 2009).

Therefore, an original preconditioning step, to first obtain the atherosclerotic lesion morphology, and then an iterative algorithm combining a dynamic watershed segmentation (DWS) method with an optimization procedure were proposed to reconstruct the transmural spatial elasticity distribution.

Three main studies were conducted in our collaborative research program to test the performance of the plaque-imaging modulography tool iMOD based on recorded RF-IVUS sequences:

- The first one was to study in vitro, using two polyvinyl alcohol (PVA) cryogel vessel phantoms, the potential of iMOD to characterize the vessel wall and to detect soft inclusions (Le Floc'h et al., 2010).
- The second one was to test ex vivo the potential of iMOD to characterize healthy rabbit aortic vessels (Deleaval, 2013).
- The third one was to test the clinical potential of iMOD to identify VPs based on RF-IVUS sequences obtained in seven patients referred for directional coronary atherectomy intervention (Le Floc'h et al., 2012).

4.1 THE MORPHO-ELASTIC BIOMECHANICAL MODEL

The iMOD algorithm was designed to calculate the elasticity map of the arterial wall from the IVUS radial strain field. An illustration of all successive steps performed in the iMOD morpho-elastic algorithm is given in Fig. 20.4.

Modified Sumi's transform (MST) criterion. We extended the Sumi and Nakayama (1998) method from its original plane stress condition to one of plane strain to define our contour detection algorithm of elastic heterogeneities. Assuming a linear isotropic elastic response between two successive frames Im^i and Im^{i+1} (see Section 2.2 of this chapter), an incompressible heterogeneous plaque medium and neglecting gravity and inertial forces, the local equation gives the following relationship:

$$\frac{\nabla E}{E} = \frac{3}{2}\,\boldsymbol{\varepsilon}^{-1}\frac{\nabla p}{E} + \mathbf{H} \text{ with } \mathbf{H} = -\boldsymbol{\varepsilon}^{-1}\nabla\cdot\varepsilon \tag{20.11a,b}$$

where E, p, and $\boldsymbol{\varepsilon}$ are the local Young's moduli, the Lagrange multiplier, and the strain tensor, respectively.

Since the Lagrange multiplier p cannot be estimated experimentally, we used the second term of the right-hand side of Eq. (20.11a) to highlight the Young's modulus discontinuity boundaries:

$$dW = \mathbf{H}\cdot\mathbf{dX} \tag{20.12}$$

where **dX** is the elementary position vector in the undeformed configuration. The amplitude of the morphologic criteria dW was computed to obtain the MST-image. In practical situations, the radial strain ε_{RR} is the most reliable estimated component of the strain tensor $\boldsymbol{\varepsilon}$ when using the LSME technique. Therefore, the criterion was simplified by neglecting the shear strain in the R-θ plane (i.e., $\varepsilon_{R\theta} = 0$). Moreover, due to the incompressibility constraint, the circumferential strain component $\varepsilon_{\theta\theta}$ was approximated by $-\varepsilon_{RR}$.

The successful morpho-elastic reconstruction maps validated a posteriori the relevance of this choice. Then, a DWS operation (Watershed function, Imaging Tool Box, MATLAB, version 7.6, the MathWorks, Natick, MA, USA) is applied to the MST-field to obtain the plaque mechanical heterogeneities, treated as preconditioning regions. We assume a uniform stiffness for each of these regions and compute their Young's moduli with an optimization process (Optimization Lab Module,

COMSOL, version 3.5, COMSOL Inc, Grenoble, France) that minimizes the root mean square (RMS) error between the radial strain field computed with a parametric finite element model (PFEM) and the IVUS radial strain field estimated by the LSME. The DWS and optimization are repeated, increasing the number of regions to account each time for smaller heterogeneities, until the RMS error between two successive iterations is below the designated threshold of 10^{-5}. A sequential quadratic programming algorithm with a numerical estimation of the gradient by the adjoint method (Gill et al., 2005) was used for the optimization procedure. Summarizing, the iMOD tool comprises three algorithms: the MST algorithm to extract a pseudo-gradient elasticity map (MST-field), the DWS segmentation procedure to extract the inclusions' contours, and the optimization algorithm that provides the Young's moduli for the detected regions. A detailed description of the plaque-imaging algorithm iMOD can be found in Le Floc'h et al. (2009).

4.2 VALIDATION OF THE MORPHO-ELASTIC RECONSTRUCTION IMAGING TOOL

Two studies were conducted to test and validate the performance of the imaging morpho-elastic reconstruction tool iMOD.

Validation study: In vitro vessel phantoms. Three vessel phantoms were fabricated from PVA cryogel, a widely used polymer material mimicking passive biological tissues. Phantom manufacturing followed the protocol described by Fromageau et al. (2007); using a 10% weight solution of PVA in water and adding a 3% weight of Sigmacell particles (Sigmacell cellulose type 50, Sigma Chemical, St Louis, MO, USA) as scatters. Polymerization was achieved by one to six freeze-thaw (F-T) cycles, depending on the mechanical properties desired for each region. Three cylindrical concentric vessel phantoms were made, one homogeneous (one F-T cycle), and the others with one and two soft inclusions (vessel wall with six F-T cycles and inclusions with one F-T cycle), respectively. Cross-sectional IVUS image sequences were acquired while the phantoms were mounted in a bench, with quasi-static pressure provided by a water column. Images at 10 different pressure steps were captured with an IVUS scanner (model In-Vision Gold, Volcano Therapeutics) equipped with a 20 MHz IVUS catheter. Images were digitalized using an external data-acquisition system (model Remora, Volcano Therapeutics). The mechanical properties of all PVA cryogel media used to fabricate our vessel phantoms were investigated by performing compression tests using a dynamic mechanical analyzer (DMA; GABO Eplexor, Ahlden, Germany, load cell of 25N, sensor sensitivity of 10^{-4} at full range).

The elasticity reconstruction performed on the homogeneous PVA cryogel phantom (phantom #1) is presented in Fig. 20.5. A computed quasi-uniform Young's modulus distribution was found with a mean value of 29.6 ± 4.0 kPa . This amplitude agrees with the measured mean amplitude of 17.6 ± 3.4 kPa found when performing DMA mechanical tests on this PVA cryogel medium.

The elasticity reconstruction conducted on the heterogeneous PVA cryogel phantom made of two soft inclusions (phantom #3) was also successfully estimated (Fig. 20.6). The imaging tool iMOD was able, not only to extract accurately the morphologies and locations of the two soft heterogeneities, but also to reasonably quantify the Young's moduli of the soft inclusions (computed $= 19.3 \pm 12.9$ vs. measured $= 17.6 \pm 3.4$ kPa) and surrounding media (computed $= 168.6 \pm 128.1$ vs. measured $= 145.4 \pm 31.8$kPa).

Interestingly, in this study we showed that the IVUS modulography algorithm iMOD was also able to highlight the nonlinear mechanical properties of the PVA by analyzing a series of successive modulograms during an increase in blood pressure. Because the mechanical property of the PVA

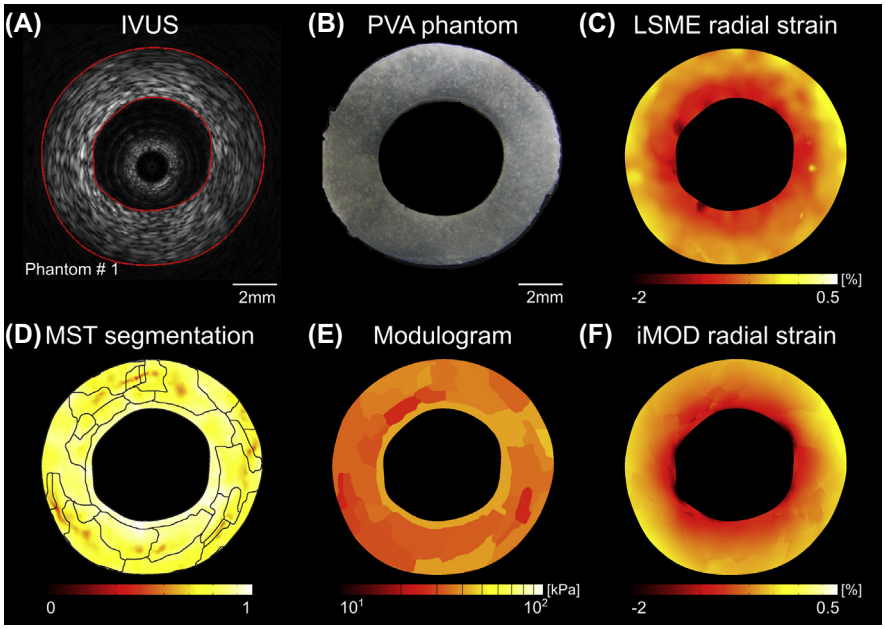

FIGURE 20.5

Performance of our elasticity reconstruction algorithm iMOD to characterize locally the mechanical properties of the homogeneous vessel phantom wall using experimental RF-IVUS images acquired with a Volcano Therapeutics REMORA IVUS system. (A) IVUS image (the red contours delimit the boundaries of the vessel wall); (B) cross-section image of the homogeneous cryogel vessel phantom; (C) measured LSME radial strain field obtained by using the Lagrangian speckle model estimator (LSME). This strain field results from two consecutive IVUS images recorded at a pressure of 0.25 and 0.5 kPa, respectively; (D) spatial pseudo-gradient elasticity field dW (Eq. 20.12) resulting from the modified Sumi's transform (MST) procedure. Contours of the elastic heterogeneity domains were obtained thanks to the dynamic watershed segmentation (DWS) method; (E) final Young's modulus map (or modulogram); (F) resulting computed radial strain map obtained when performing a finite element simulation with the final modulogram presented in (E). Qualitatively, there is a noticeable good agreement between the PFEM-computed (F) and IVUS-measured (C) radial strain distributions.

Adapted from Le Floc'h, S., Cloutier, G., Finet, G., Tracqui, P., Pettigrew, R.I., Ohayon, J., 2010. On the potential of a new IVUS elasticity modulus imaging approach for detecting vulnerable atherosclerotic coronary plaques: in vitro vessel phantom study. Phys Med Biol 55, 5701–5721. © Institute of Physics and Engineering in Medicine. Reproduced by permission of IOP Publishing. All rights reserved.

cryogel is nonlinear, we investigated the potential of the modulography algorithm to sense the strain hardening of the gel by taking advantage of the series of cross-sectional IVUS images acquired from the phantoms #2 and #3 at each pressure step. A series of 10 modulograms were computed by considering 10 sets of two successive IVUS images acquired during the pressure-loading period. By using this protocol, we successfully quantified the increase in Young's moduli with strain from all computed modulograms (see Figs. 8 and 9 in Le Floc'h et al. (2010)).

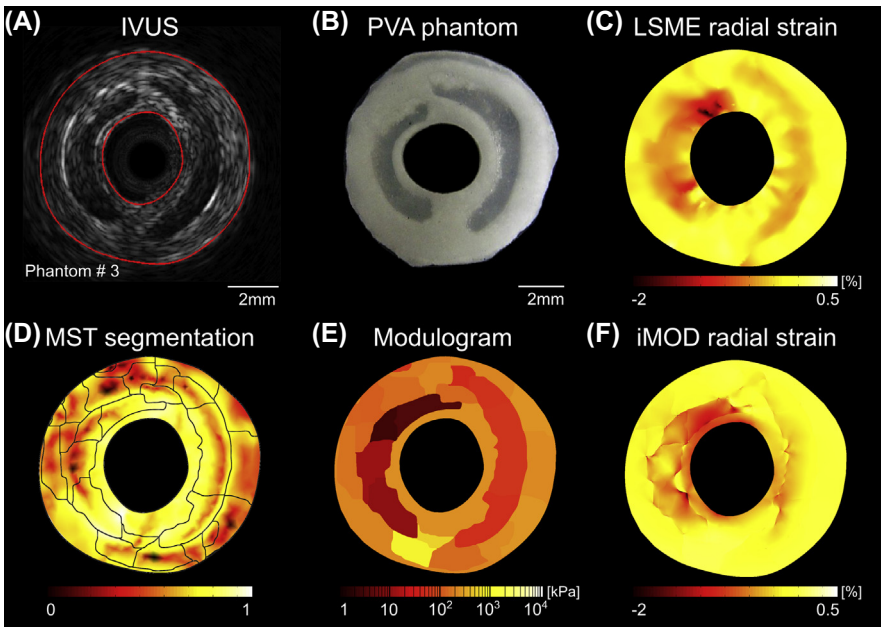

FIGURE 20.6

Performance of our elasticity reconstruction algorithm iMOD to characterize locally the mechanical properties of the heterogeneous vessel phantom wall with two soft inclusions using experimental RF-IVUS images acquired with a Volcano Therapeutics REMORA IVUS system. (A) IVUS image; (B) cross-section image of the heterogeneous cryogel vessel phantom; (C) measured LSME radial strain field resulting from two consecutive IVUS images recorded pressures of 4 and 4.5 kPa, respectively; (D) spatial pseudo-gradient elasticity field with the potential contours of the elastic heterogeneity domains with contours of the elastic heterogeneity domains; (E) final Young's modulus map (or modulogram); (F) resulting computed radial strain map obtained when performing a finite element simulation with the final modulogram presented in (E). Qualitatively, there is a noticeable good agreement between the PFEM-computed (F) and IVUS-measured (C) radial strain distributions.

Adapted from Le Floc'h, S., Cloutier, G., Finet, G., Tracqui, P., Pettigrew, R.I., Ohayon, J., 2010. On the potential of a new IVUS elasticity modulus imaging approach for detecting vulnerable atherosclerotic coronary plaques: in vitro vessel phantom study. Phys Med Biol 55, 5701–5721.

Animal study: Ex vivo experiment. For this study, we used the same rabbit population presented earlier (see Section 3.4 of this chapter). In Fig. 20.7 we present a preliminary result showing the capabilities of our elasticity reconstruction algorithm iMOD to characterize locally the Young's modulus of a healthy aortic wall of a Watanabe rabbit using experimental RF images acquired with an IVUS system. Our result shows that the mean modulogram amplitude (57.9 ± 49.2 kPa, Fig. 20.7E) agrees quite well with the mean Young's modulus of 53.4 ± 60.1 kPa obtained by performing AFM mechanical tests on n = 24 random locations of the vessel wall and by assuming the arterial wall as homogeneous, isotropic, and quasi-incompressible.

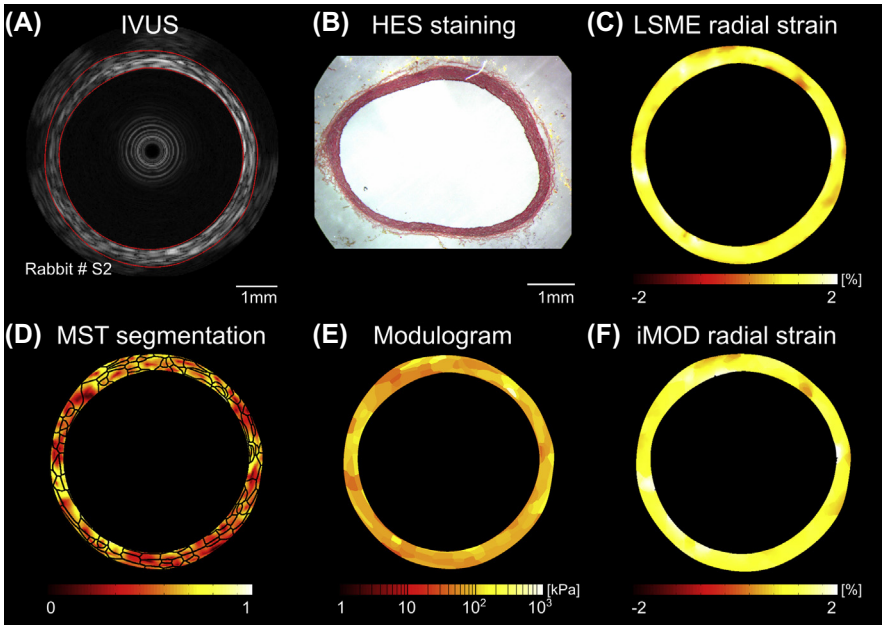

FIGURE 20.7

Performance of our elasticity reconstruction algorithm iMOD to characterize ex vivo the mechanical properties of a healthy aortic wall of a Watanabe rabbit (Rabbit #S2) using experimental RF-IVUS images acquired with a Boston Scientific GALAXY2 IVUS system. (A) IVUS image (the red contours delimit the boundaries of the vessel wall); (B) trichrome, hematoxylin, erythosine, safran (HES) staining of the healthy aortic wall where nucleus, cytoplasm, and fibrosis are in blue, pink, and yellow, respectively (no atherosclerotic lesion was observed); (C) measured LSME radial strain field resulting from two consecutive IVUS images recorded at pressures of 2.3 and 2.23 kPa, respectively; (D) spatial pseudo-gradient elasticity field dW (Eq. 20.12) resulting from the modified Sumi's transform (MST) procedure. Contours of the elastic heterogeneity domains were obtained thanks to the dynamic watershed segmentation (DWS) method; (E) final Young's modulus map (or modulogram); (F) resulting computed radial strain map obtained when performing a finite element simulation with the final modulogram presented in (E).

5. FROM MODEL TO PATIENT

The performance of the elasticity reconstruction method iMOD was investigated on IVUS sequences obtained from seven patients scheduled for directional coronary atherectomy (DCA) intervention (Le Floc'h et al., 2012). The protocol was approved by the Review Ethical Committee of Sendai University Hospital and patients gave their written consent. Imaging sequences consisting of 30 frames were recorded with a 40 MHz IVUS catheter connected to a Galaxy II echograph (Boston Scientific, Natick, MA, USA). Because no pressure measurements were performed during the clinical protocol, the blood pressure differential was calculated by assuming a linear variation between diastolic and systolic pressures.

During the DCA procedure, arterial sections were excised using a specially designed catheter (Flexicut, Guidant Corporation, Santa Clara, CA, USA). Samples were fixed in 10% formalin, embedded in paraffin and cut into 4 μm slices using a microtome. Then they were stained with Elastica-Masson's trichrome to quantify the constituents of the seven excised lesions.

Based on the recorded RF-IVUS-sequences, 29 and 28 modulograms were computed for patients #9 and #11, respectively. These two data sets show that the diastolic phase of the cardiac cycle is the best time interval to obtain reproducible modulograms. Figs. 20.8 and 20.9 display the representative

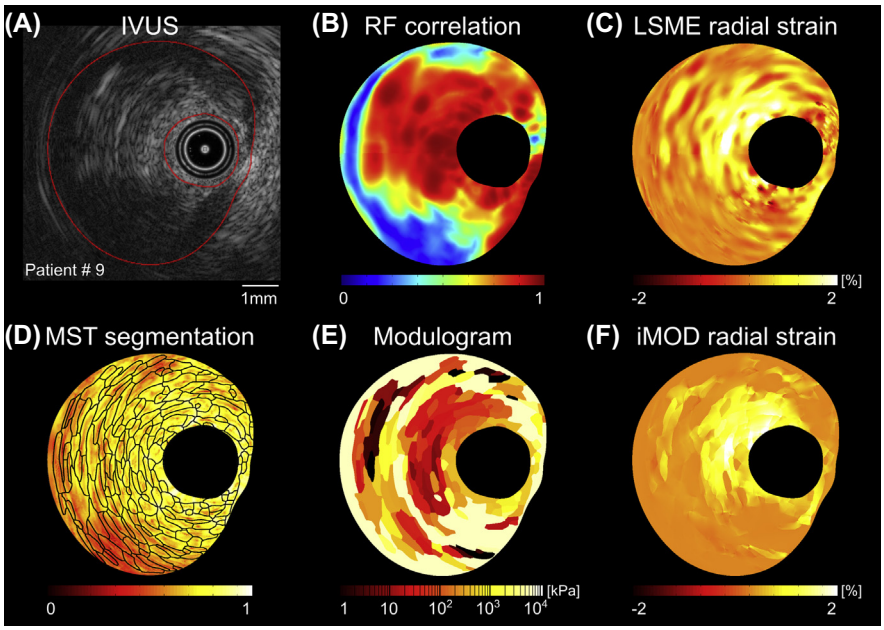

FIGURE 20.8

Performance of our elasticity reconstruction algorithm iMOD to characterize in vivo the mechanical properties of a human atherosclerotic plaque (patient #9) using experimental RF-IVUS images acquired with a Boston Scientific GALAXY2 IVUS system. (A) IVUS image (the red contours delimit the boundaries of the vessel wall); (B) spatial distribution of the RF-correlation coefficient; (C) measured LSME radial strain field obtained by using the Lagrangian speckle model estimator (LSME); (D) spatial pseudo-gradient elasticity field dW (Eq. 20.12) resulting from the modified Sumi's transform (MST) procedure. Contours of the elastic heterogeneity domains were obtained thanks to the dynamic watershed segmentation (DWS) method; (E) final Young's modulus map (or modulogram); (F) resulting computed radial strain map obtained when performing a finite element simulation with the final modulogram presented in (E). Qualitatively, there is a noticeable good agreement between the PFEM-computed (F) and IVUS-measured (C) radial strain distributions.

Adapted from Le Floc'h, S., Cloutier, G., Saijo, Y., Finet, G., Yazdani, S.K., Deleaval, F., et al., 2012. A four-criterion selection procedure for atherosclerotic plaque elasticity reconstruction based on in vivo coronary intravascular ultrasound radial strain sequences. Ultrasound Med Biol 38 (12), 2084–2097.

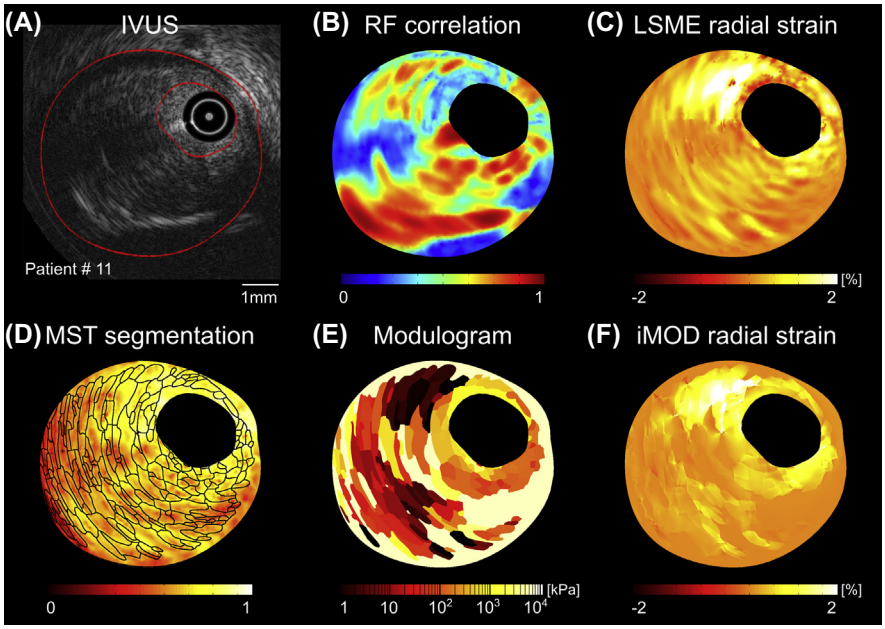

FIGURE 20.9

Performance of our elasticity reconstruction algorithm iMOD to characterize in vivo the mechanical properties of a human atherosclerotic plaque (patient #11) using experimental RF-IVUS images acquired with a Boston Scientific GALAXY2 IVUS system. (A) IVUS image; (B) spatial distribution of the RF-correlation coefficient; (C) measured LSME radial strain field; (D) spatial pseudo-gradient elasticity MST field with elastic heterogeneity domains; (E) final Young's modulus map (or modulogram); (F) computed radial strain map.

Adapted from Le Floc'h, S., Cloutier, G., Saijo, Y., Finet, G., Yazdani, S.K., Deleaval, F., et al., 2012. A four-criterion selection procedure for atherosclerotic plaque elasticity reconstruction based on in vivo coronary intravascular ultrasound radial strain sequences. Ultrasound Med Biol 38 (12), 2084–2097.

modulograms, RF-correlation coefficient, MST, and IVUS-estimated and PFEM-computed radial strain maps obtained for these patients. Notice that a low value of the RF-correlation coefficient indicates a poor estimate of displacement due to either high acoustic noise or a low signal-to-noise ratio. Qualitatively, we found noticeable good agreements between the PFEM-computed and IVUS-measured radial strain distributions (see Fig. 20.8C and F and 20.9C and F).

Correlations between the patient's modulogram and the histological analysis of the associated excised lesion were considered relevant (see Fig. 20.8 in Le Floc'h et al. (2012)), but not enough (due the small number of studied patients) to validate our plaque-imaging tools. Consequently, even if the iPALP and iMOD imaging techniques show original and promising results, new in vivo clinical studies in animals and complementary clinical studies are still needed to strongly validate these two techniques. Therefore, a new in vivo animal research program performed on pathological coronaries of adult pigs has started in our laboratories.

6. RELEVANCE OF THE TWO IMAGING TECHNIQUES AND THEIR LIMITATIONS

6.1 WHEN TO USE THE PALPOGRAPHY OR MODULOGRAPHY TECHNIQUE

Compared to modulography, palpography is a faster imaging technique since it requires only direct FE calculations to compute the palpogram. Although the palpography technique is sufficient to detect and identify VPs, it does not allow us to characterize the degree of vulnerability of the imaged atherosclerotic lesion (i.e., to quantify PCS). Only the modulography technique allows it. These two algorithms are therefore complementary and should be used in clinical practice as follows. The interventional cardiologist could explore the coronary branches using the palpography mode and visualize in detail the content of the coronary cross section of interest by activating the modulography mode.

6.2 LIMITATIONS OF THE TWO IMAGING TECHNIQUES

Several limitations deserve to be pointed out for both imaging techniques, even if this chapter describes promising results. First, an important technical limitation remains the necessity to record the blood pressure on patients during the IVUS acquisition sequences. Since blood pressure was not measured for the previous clinical study (see Section 5), the modulograms were obtained by assuming a bilinear pressure-time evolution during the cardiac cycle (varying between the end systolic and end diastolic pressure amplitudes of the patient measured in clinical routine). Second, the influence of residual stress/strain (RS/S) (see Chapter 19 of this volume) have been completely ignored in these studies. Indeed, neglecting RS/S in structural analysis would bias the determination of the physiological spatial distribution of stresses but not the characterization of estimated mechanical properties using palpography and modulography techniques. Finally, in order to take into account the dynamics of the 2D IVUS sequence, our computational FE simulations were conducted in two dimensions by assuming the plane strain constraint. This assumption remains reasonable since the plaque length is large with regard to the radial dimension, which is often the case for mature VPs with high degree of stenosis (Ohayon et al., 2005).

7. RELEVANCE FOR CLINICAL AND PHARMACOLOGICAL APPLICATIONS

Research has evidenced that plaque rupture depends on a complex combination of mechanical and biological processes such as plaque erosion (Bentzon et al., 2014), macrophage-induced tissue degradation (Naghavi et al., 2003), as well as other biological mechanisms linked to cellular inflammatory reaction (Bentzon et al., 2014; Newby, 2006; Arroyo and Lee, 1999). Therefore, the search for rupture biomarkers that merge both the mechanical and biological characteristics of vulnerable plaques is a promising concept.

The stability of the plaque can be attributed to the mechanical properties of its components. A study by Finet et al. (2004) shows that the peak cap stress—a key predictor of plaque failure—is very sensitive not only to the thickness of the cap, but also to the elasticity gradient between the necrotic core and the fibrous cap. This demonstrates that even a small variation in structural properties can tilt a vulnerable plaque from stability to instability. The effects that current statin-based treatments

(Du et al., 2018; Mazzone et al., 2018; Nozue et al., 2012; Libby et al., 2002) and other emerging drugs (Nicholls et al., 2016) have on atherosclerotic lesions are still unclear. By using the proposed modulography and palpography imaging techniques, clinicians could evaluate the change in mechanical properties induced on the plaque by drug treatments, and possibly develop appropriate therapies for their patients.

ACKNOWLEDGMENTS

The authors thank Yoshifumi Saijo (Tohoku University, Sendai, Japan) for allowing us to use the RF-IVUS sequences of the patients referred for a directional coronary atherectomy intervention in Sendai University hospital, Saami K. Yazdani (University of South Alabama, Mobile, AL, USA), Manuel Lagache (University Savoie Mont-Blanc, Chambéry, France), Jean-Louis Martiel (University Grenoble-Alpes, Grenoble, France), and Alex Elias-Zuñiga (Technologic Institutes of Monterrey, NL Mexico) for helpful discussions. A. Gómez and J. Ohayon thank the Mexican Science and Technology Council (CONACYT) and Nuevo-León's Innovation and Technology Transfer Institute (I2T2). A. Gómez held a doctoral fellowship from CONACYT (2016−19). This research was partially supported by a joint international program of the Agence Nationale de la Recherche (ANR) grant MELANII project # 09-BLAN-0423 (J. Ohayon) and of the Natural Sciences and Engineering Research Council of Canada (NSERC) strategic grant # STPGP-381136-09 (G. Cloutier). The iPALP and iMOD technological transfer programs are supported by the SATT Linksium Grenoble Alpes 2018−19 # 180002M (J. Ohayon and G. Finet).

REFERENCES

Abela, O.G., Ahsan, C.H., Alreefi, F., Salehi, N., Baig, I., Janoudi, A., Abela, G.S., 2016. Plaque rupture and thrombosis: the value of the atherosclerotic rabbit model in defining the mechanism. Curr Atherosclerosis Rep 18 (6), 29.

Abran, M., Cloutier, G., Cardinal, M.H.R., Chayer, B., Tardif, J.C., Lesage, F., 2014. Development of a photoacoustic, ultrasound and fluorescence imaging catheter for the study of atherosclerotic plaque. IEEE Trans Biomed Circuits Syst 8 (5), 696−703.

Arroyo, L.H., Lee, R.T., 1999. Mechanisms of plaque rupture: mechanical and biologic interactions. Cardiovasc Res 41 (2), 369−375.

Baldewsing, R.A., Mastik, F., Schaar, J.A., Serruys, P.W., van der Steen, A.F.W., 2005. Robustness of reconstructing the Young's modulus distribution of vulnerable atherosclerotic plaques using a parametric plaque model. Ultrasound Med Biol 31 (12), 1631−1645.

Baldewsing, R.A., Mastik, F., Schaar, J.A., Serruys, P.W., van der Steen, A.F.W., 2006. Young's modulus reconstruction of vulnerable atherosclerotic plaque components using deformable curves. Ultrasound Med Biol 32 (2), 201−210.

Baldewsing, R.A., Schaar, J.A., Mastik, F., van der Steen, A.F.W., 2007. Local elasticity imaging of vulnerable atherosclerotic coronary plaques. Adv Cardiol 44, 35−61.

Baldewsing, R.A., Danilouchkine, M.G., Mastik, F., Schaar, J.A., Serruys, P.W., van der Steen, A.F.W., 2008. An inverse method for imaging the local elasticity of atherosclerotic coronary plaques. IEEE Trans Inf Technol Biomed 12 (3), 277−289.

Bentzon, J.F., Otsuka, F., Virmani, R., Falk, E., 2014. Mechanisms of plaque formation and rupture. Circ Res 114 (12).

Berthelot, J.-M., 1999. Elastic behavior of an orthotropic composite. In: Composite Materials: Mechanical Behavior and Structural Analysis, pp. 186−194.

Bonet, J., Wood, R.D., 1997. Nonlinear Continuum Mechanics for Finite Element Analysis. Cambridge University Press.

Bourantas, C.V., Jaffer, F.A., Gijsen, F.J., Van Soest, G., Madden, S.P., Courtney, B.K., et al., 2017. Hybrid intravascular imaging: recent advances, technical considerations, and current applications in the study of plaque pathophysiology. Eur Heart J 38, 400−412.

Bouvier, A., Deleaval, F., Doyley, M.M., Yazdani, S.K., Finet, G., Le Floc'h, S., et al., 2013. A direct vulnerable atherosclerotic plaque elasticity reconstruction method based on an original material-finite element formulation: theoretical framework. Phys Med Biol 58 (23), 8457−8476.

Cardoso, L., Weinbaum, S., 2018. Microcalcifications, their genesis, growth, and biomechanical stability in fibrous cap rupture. Adv Exp Med Biol 1097, 129−155.

Cardoso, F.M., Matsumoto, M.M.S., Furuie, S.S., 2012. Edge-preserving speckle texture removal by interference-based speckle filtering followed by anisotropic diffusion. Ultrasound Med Biol 38 (8), 1414−1428.

Cavalcante, J.L., Larose, E., 2016. Intravascular MRI for plaque characterization: are we close to reality? Curr Cardiol Rep 18 (9), 89.

Céspedes, E.I., De Korte, C.L., Van Der Steen, A.F.W., 2000. Intraluminal ultrasonic palpation: assessment of local and cross-sectional tissue stiffness. Ultrasound Med Biol 26 (3), 385−396.

Chagnon, G., Ohayon, J., Martiel, J.-L., Favier, D., 2017. Hyperelasticity modeling for incompressible passive biological tissues. In: Biomechanics of Living Organs. Elsevier, pp. 3−30.

Cheng, J.M., Garcia-Garcia, H.M., De Boer, S.P.M., Kardys, I., Heo, J.H., Akkerhuis, K.M., et al., 2014. In vivo detection of high-risk coronary plaques by radiofrequency intravascular ultrasound and cardiovascular outcome: results of the ATHEROREMO-IVUS study. Eur Heart J 35, 639−947.

Sumi, C., Nakayama, K., 1998. A robust numerical solution to reconstruct a globally relative shear modulus distribution from strain measurements. IEEE Trans Med Imag 17 (3), 419−428.

De Korte, C.L., Carlier, S.G., Mastik, F., Doyley, M.M., Van Der Steen, A.F.W., Serruysa, P.W., Bom, N., 2002. Morphological and mechanica0l information of coronary arteries obtained with intravascular elastography: feasibility study in vivo. Eur Heart J 23, 405−413.

Deleaval, F., Bouvier, A., Finet, G., Cloutier, G., Yazdani, S.K., Le Floc'h, S., et al., 2013. The intravascular ultrasound elasticity-palpography technique revisited: a reliable tool for the in vivo detection of vulnerable coronary atherosclerotic plaques. Ultrasound Med Biol 39 (8), 1469−1481.

Deleaval, F., 2013. Caractérisation des propriétés mécaniques de la plaque d'athérome à partir de données échographiques endovasculaires: la technique de palpographie revisitée (Ph.D. report). University Grenoble Alpes, France.

Doyley, M.M., 2012. Model-based elastography: a survey of approaches to the inverse elasticity problem. Phys Med Biol 57 (3), R35−R73.

Du, X., Zhang, S., Liu, L., November 15, 2018. Statin therapy contributes to plaque-stability by increasing the presence of calcification of plaque. Int J Cardiol 271, 24.

Farb, A., Burke, A.P., Tang, A.L., Liang, T.Y., Mannan, P., Smialek, J., Virmani, R., 1996. Coronary plaque erosion without rupture into a lipid core. A frequent cause of coronary thrombosis in sudden coronary death. Circulation 93 (7), 1354−1363.

Fayad, Z.A., Fuster, V., Nikolaou, K., Becker, C., 2002. Computed tomography and magnetic resonance imaging for noninvasive coronary angiography and plaque imaging. Circulation 106 (15), 2026−2034.

Finet, G., Ohayon, J., Rioufol, G., 2004. Biomechanical interaction between cap thickness, lipid core composition and blood pressure in vulnerable coronary plaque: impact on stability or instability. Coron Artery Dis 15, 13−20.

Fleg, J.L., Stone, G.W., Fayad, Z.A., Granada, J.F., Hatsukami, T.S., Kolodgie, F.D., et al., 2012. Detection of high-risk atherosclerotic plaque: report of the NHLBI Working Group on current status and future directions. JACC Cardiovasc Imag 5 (9), 941−955.

Fromageau, J., Brusseau, E., Vray, D., Gimenez, G., Delachartre, P., 2003. Characterization of PVA cryogel for intravascular ultrasound elasticity imaging. IEEE Trans Ultrason Ferroelectr Freq Control 50 (10), 1318–1324.

Fromageau, J., Gennisson, J.-L., Schmitt, C., Maurice, R.L., Mongrain, R., Cloutier, G., 2007. Estimation of polyvinyl alcohol cryogel mechanical properties with four ultrasound elastography methods and comparison with gold standard testings. IEEE Trans Ultrason Ferroelectr Freq Control 54 (3), 498–509.

Gessert, N., Lutz, M., Heyder, M., Latus, S., Leistner, D.M., Abdelwahed, Y.S., Schlaefer, A., 2018. Automatic plaque detection in IVOCT pullbacks using convolutional neural networks. IEEE Trans Med Imag 38 (2), 426–434.

Gill, P.E., Murray, W., Saunders, M.A., 2005. SNOPT: an SQP algorithm for large-scale constrained optimization. SIAM Rev 47 (1), 99–131.

Gómez, A., Tacheau, A., Finet, G., Lagache, M., Martiel, J.-L., Floc'h, S.L., et al., 2019. Intraluminal ultrasonic palpation imaging technique revisited for anisotropic characterization of healthy and atherosclerotic coronary arteries: a feasibility study. Ultrasound Med Biol 45 (1), 35–49.

Hasegawa, M., Watanabe, Y., 1988. Rheological properties of the thoracic aorta in normal and WHHL rabbits. Biorheology 25, 147–156.

Holzapfel, G.A., Sommer, G., Gasser, C.T., Regitnig, P., 2005. Determination of layer-specific mechanical properties of human coronary arteries with nonatherosclerotic intimal thickening and related constitutive modeling. Am J Physiol Heart Circ Physiol 289 (5), H2048–H2058.

Holzapfel, G.A., 2000. Nonlinear Solid Mechanics: A Continuum Approach for Engineering. Wiley.

Jensen, J.A., Svendsen, N.B., 1992. Calculation of pressure fields from arbitrarily shaped, apodized, and excited ultrasound transducers. IEEE Trans Ultrason Ferroelectr Freq Control 39 (2), 262–267.

Kanai, H., Hasegawa, H., Ichiki, M., Tezuka, F., Koiwa, Y., 2003. Elasticity imaging of atheroma with transcutaneous ultrasound. Circulation 107 (24), 3018–3021.

Khalil, A.S., Bouma, B.E., Kaazempur Mofrad, M.R., 2006. A combined FEM/genetic algorithm for vascular soft tissue elasticity estimation. Cardiovasc Eng 6 (3), 93–102.

Kim, K., Weitzel, W.F., Rubin, J.M., Xie, H., Chen, X., O'Donnell, M., 2004. Vascular intramural strain imaging using arterial pressure equalization. Ultrasound Med Biol 30 (6), 761–771.

Larose, E., Yeghiazarians, Y., Libby, P., Yucel, E.K., Aikawa, M., Kacher, D.F., et al., 2005. Characterization of human atherosclerotic plaques by intravascular magnetic resonance imaging. Circulation 112, 2324–2331.

Le Floc'h, S., Ohayon, J., Tracqui, P., Finet, G., Gharib, A.M., Maurice, R.L., et al., 2009. Vulnerable atherosclerotic plaque elasticity reconstruction based on a segmentation-driven optimization procedure using strain measurements: theoretical framework. IEEE Trans Med Imag 28 (7), 1126–1137.

Le Floc'h, S., Cloutier, G., Finet, G., Tracqui, P., Pettigrew, R.I., Ohayon, J., 2010. On the potential of a new IVUS elasticity modulus imaging approach for detecting vulnerable atherosclerotic coronary plaques: in vitro vessel phantom study. Phys Med Biol 55, 5701–5721.

Le Floc'h, S., Cloutier, G., Saijo, Y., Finet, G., Yazdani, S.K., Deleaval, F., et al., 2012. A four-criterion selection procedure for atherosclerotic plaque elasticity reconstruction based on in vivo coronary intravascular ultrasound radial strain sequences. Ultrasound Med Biol 38 (12), 2084–2097.

Lee, R., Grodzinsky, A., Frank, E., Kamm, R., Schoen, F., Lee, R.T., et al., 1991. Structure-dependent dynamic mechanical behavior of fibrous caps from human structure-dependent dynamic mechanical behavior of fibrous caps from human atherosclerotic plaques. Circulation 83, 1764–1770.

Lee, R.T., Loree, H.M., Cheng, G.C., Lieberman, E.H., Jaramillo, N., Schoen, F.J., 1993. Computational structural analysis based on intravascular ultrasound imaging before in vitro angioplasty: prediction of plaque fracture locations. J Am Coll Cardiol 21 (3), 777–782.

Libby, P., Ridker, P.M., Maseri, A., 2002. Inflammation and atherosclerosis. Circulation 105 (9), 1135–1143.

Loree, H.M., Kamm, R.D., Stringfellow, R.G., Lee, R.T., 1992. Effects of fibrous cap thickness on peak circumferential stress in model atherosclerotic vessels. Circ Res 71 (4), 850–858.

Loree, H.M., Tobias, B.J., Gibson, L.J., Kamm, R.D., Small, D.M., Lee, R.T., 1994. Mechanical properties of model atherosclerotic lesion lipid pools. Arterioscler Thromb 14 (2), 230–234.

Luo, J., Ying, K., Bai, J., 2006. Elasticity reconstruction for ultrasound elastography using a radial compression: an inverse approach. Ultrasonics 44, e195–e198.

Majdouline, Y., Ohayon, J., Keshavarz-Motamed, Z., Roy Cardinal, M.H., Garcia, D., Allard, L., et al., 2014. Endovascular shear strain elastography for the detection and characterization of the severity of atherosclerotic plaques: in vitro validation and in vivo evaluation. Ultrasound Med Biol 40 (5), 890–903.

Maldonado, N., Kelly-Arnold, A., Cardoso, L., Weinbaum, S., 2013. The explosive growth of small voids in vulnerable cap rupture; cavitation and interfacial debonding. J Biomech 46 (2), 396–401.

Matsumoto, T., Abe, H., Ohashi, T., Kato, Y., Sato, M., 2002. Local elastic modulus of atherosclerotic lesions of rabbit thoracic aortas measured by micropipette aspiration method. Physiol Meas 23, 635–648.

Maurice, R.L., Ohayon, J., Finet, G., Cloutier, G., 2004a. Adapting the Lagrangian speckle model estimator for endovascular elastography: theory and validation with simulated radio-frequency data. J Acoust Soc Am 116 (2), 1276–1286.

Maurice, R.L., Ohayon, J., Frétigny, Y., Bertrand, M., Soulez, G., Cloutier, G., 2004b. Noninvasive vascular elastography: theoretical framework. IEEE Trans Med Imag 23 (2), 164–180.

Mazzone, A., Clemente, A., Chiappino, D., Berti, S., Vassalle, C., 2018. Double face of statins at the crossroad of coronary atherosclerotic plaque and aortic valve calcification? JACC Cardiovasc Imag 11 (12), 1930–1931.

Naghavi, M., Libby, P., Falk, E., Casscells, S.W., Litovsky, S., Rumberger, J., et al., 2003. From vulnerable plaque to vulnerable patient: a call for new definitions and risk assessment strategies: part I. Circulation 108 (14), 1664–1672.

Nayak, R., Huntzicker, S., Ohayon, J., Carson, N., Dogra, V., Schifitto, G., Doyley, M.M., 2017. Principal strain vascular elastography: simulation and preliminary clinical evaluation. Ultrasound Med Biol 43 (3), 682–699.

Newby, A.C., 2006. Do metalloproteinases destabilize vulnerable atherosclerotic plaques? Curr Opin Lipidol 17 (5), 556–561.

Nicholls, S.J., Puri, R., Anderson, T., Ballantyne, C.M., Cho, L., Kastelein, J.J.P., et al., 2016. Effect of evolocumab on progression of coronary disease in statin-treated patients. J Am Med Assoc 316 (22), 2373.

Nozue, T., Yamamoto, S., Tohyama, S., Umezawa, S., Kunishima, T., Sato, A., et al., 2012. Statin treatment for coronary artery plaque composition based on intravascular ultrasound radiofrequency data analysis. Am Heart J 163 (2), 191–199.e1.

Ohayon, J., Teppaz, P., Finet, G., Rioufol, G., 2001. In-vivo prediction of human coronary plaque rupture location using intravascular ultrasound and the finite element method. Coron Artery Dis 12 (8).

Ohayon, J., Finet, G., Treyve, F., Rioufol, G., Dubreuil, O., 2005. A three-dimensional finite element analysis of stress distribution in a coronary atherosclerotic plaque: in-vivo prediction of plaque rupture location. In: Payan, Y. (Ed.), Biomechanics Applied to Computer Assisted Surgery. Research Signpost, Kerala, pp. 225–241.

Ohayon, J., Finet, G., Gharib, A.M., Herzka, D.A., Tracqui, P., Heroux, J., et al., 2008. Necrotic core thickness and positive arterial remodeling index: emergent biomechanical factors for evaluating the risk of plaque rupture. AJP Heart Circ Physiol 295 (2), H717–H727.

Ohayon, J., Mesnier, N., Broisat, A., Toczek, J., Riou, L., Tracqui, P., 2012. Elucidating atherosclerotic vulnerable plaque rupture by modeling cross substitution of ApoE−/− mouse and human plaque components stiffnesses. Biomech Model Mechanobiol 11 (6), 801–813.

Poree, J., Chayer, B., Soulez, G., Ohayon, J., Cloutier, G., 2017. Noninvasive vascular modulography method for imaging the local elasticity of atherosclerotic plaques: simulation and in vitro vessel phantom study. IEEE Trans Ultrason Ferroelectr Freq Control 64 (12), 1805–1817.

Richards, M.S., Doyley, M.M., 2011. Investigating the impact of spatial priors on the performance of model-based IVUS elastography. Phys Med Biol 56 (22), 7223−7246.

Rioufol, G., Finet, G., Ginon, I., André-Fouët, X., Rossi, R., Vialle, E., et al., 2002. Multiple atherosclerotic plaque rupture in acute coronary syndrome: a three-vessel intravascular ultrasound study. Circulation 106, 804−808.

Roy Cardinal, M.H, Meunier, J., Soulez, G., Maurice, R.L., Therasse, E., Cloutier, G., 2006. Intravascular ultrasound image segmentation: A three dimensional fast-marching method based on gray level distributions. IEEE Trans Med Imag 25, 590−601.

Sinclair, H., Bourantas, C., Bagnall, A., Mintz, G.S., Kunadian, V., 2015. OCT for the identification of vulnerable plaque in acute coronary syndrome. JACC Cardiovasc Imag 8 (2), 198−209.

Soualmi, L., Bertrand, M., Mongrain, R., Tardif, J.-C., 1997. Forward and inverse problems in endovascular elastography. In: Acoustical Imaging. Springer, New York, NY. Boston, MA, pp. 203−209.

Tacheau, A., Le Floc'h, S., Finet, G., Doyley, M.M., Pettigrew, R.I., Cloutier, G., Ohayon, J., 2016. The imaging modulography technique revisited for high-definition intravascular ultrasound: theoretical framework. Ultrasound Med Biol 42 (3), 727−741.

Thim, T., Hagensen, M.K., Wallace-Bradley, D., Granada, J.F., Kaluza, G.L., Drouet, L., et al., 2010. Unreliable assessment of necrotic core by virtual histology intravascular ultrasound in porcine coronary artery disease. Circ Cardiovasc Imag 3 (4), 384−391.

Tracqui, P., Broisat, A., Toczek, J., Mesnier, N., Ohayon, J., Riou, L., 2011. Mapping elasticity moduli of atherosclerotic plaque in situ via atomic force microscopy. J Struct Biol 174 (1), 115−123.

Virmani, R., Kolodgie, F.D., Burke, A.P., Farb, A., Schwartz, S.M., 2000. Lessons from sudden coronary death: a comprehensive morphological classification scheme for atherosclerotic lesions. Arterioscler Thromb Vasc Biol 20 (5), 1262−1275.

Virmani, R., 2011. Are our tools for the identification of TCFA ready and do we know them? JACC Cardiovasc Imag 4 (6), 656−658.